Eur. Phys. J. C 52, 397–411 (2007)
DOI 10.1140/epjc/s10052-007-0397-1

THE EUROPEAN
PHYSICAL JOURNAL C

Regular Article – Theoretical Physics

On MSSM charged Higgs-boson production in association with an electroweak W boson at electron–positron colliders

O. Brein[1,a], T. Hahn[2]

[1] Institute for Particle Physics Phenomenology, University of Durham, South Rd., DH1 3LE, Durham, UK
[2] Max-Planck-Institut für Physik, Föhringer Ring 6, 80805 München, Germany

Received: 1 June 2007 / Revised version: 9 July 2007 /

Abstract. We present a calculation of the cross section for the process $e^+e^- \to W^\pm H^\mp$ in the minimal supersymmetric standard model (MSSM) and the two Higgs doublet model (THDM). We study the basic features of the MSSM prediction for some distinctive parameter scenarios. We find large effects from virtual third-generation squarks for scenarios with large mixing, which can lead to a cross section vastly different from a THDM with identical Higgs sector parameters. We investigate this interesting behaviour in more detail by thoroughly scanning the MSSM parameter space for regions of large cross section. For a charged Higgs boson too heavy to be pair produced at a future high-energy electron–positron collider it turns out that a large MSSM cross section with a good chance of observation is linked to a squark mass scale below 600 GeV and a considerable amount of mixing in either the stop and sbottom sector.

1 Introduction

The discovery potential of the CERN large hadron collider (LHC) should be sufficient to resolve the issue of the existence of a neutral Higgs boson, especially of the standard model Higgs boson [1–4]. An electron–positron collider would, however, serve as an ideal tool to measure the properties of neutral Higgs bosons very precisely [5–7]. To discover a charged Higgs boson, $H^\pm$, on the other hand, is much harder at the LHC [1–4, 8, 9], especially if the $H^\pm$ is substantially heavier than the top quark. The reason for this is the dominant decay of the $H^\pm$ bosons into heavy quarks ($t\bar{b}$ or $\bar{t}b$), which leads to hadronic signatures that are hard to distinguish from QCD background events and which forces one either to rely on the less probable decay $H^\pm \to \tau\nu$ or to accumulate a lot of statistics during several years of running at high luminosity in order to claim discovery. Actually, the strong dependence of the production cross sections on the ratio of vacuum expectation values in the Higgs sector, $v_2/v_1 = \tan\beta$, makes it almost impossible to discover the charged Higgs boson at the LHC in a wedge-shaped region of intermediate $\tan\beta$-values in the $\tan\beta$–$m_{H^\pm}$ plane if it is heavier than the top-quark [1–4, 8, 9]. This non-discovery range includes $4 \lesssim \tan\beta \lesssim 12$ at $m_{H^\pm} = 250$ GeV and widens continuously to e.g. $2 \lesssim \tan\beta \lesssim 40$ at $m_{H^\pm} = 650$ GeV [8, 9].

At an e^+e^- collider with a centre-of-mass energy $\sqrt{s}$, the main production process for charged Higgs bosons is pair production ($e^+e^- \to H^+H^-$), which is mediated mainly via photon- and Z-exchange in the s-channel. The pair-production cross section is almost independent of $\tan\beta$ and, owing to the colourless initial state, Higgs-boson signatures from decays into heavy quarks are not obscured by enormous amounts of QCD background events, like at the LHC. Therefore, detection of charged Higgs bosons via pair production should be possible in the whole $m_{H^\pm}$–$\tan\beta$ plane up to a mass limit somewhat below $\sqrt{s}/2$. If the collider energy is not sufficient for pair production (i.e. $\sqrt{s} < 2m_{H^\pm}$), the only way to extend the search for the charged Higgs boson to higher masses is to try to observe its single production in association with lighter particles. The most relevant processes that have been studied in the literature are the tree-level processes $e^+e^- \to H^\pm\tau\nu$ [10–13] and $e^+e^- \to H^\pm tb$ [13–16] and the loop-induced processes $e^+e^- \to H^\pm e\nu$ [13, 17, 18] and $e^+e^- \to W^\pm H^\mp$ [13, 19–24]. Most of the studies are done in the framework of THDM with parameters fixed at MSSM values, except for [22, 23], which study $W^\pm H^\mp$ production in the general THDM, [19, 20, 24], which study the same process in the full MSSM, and [18], which includes virtual sfermion contributions for the cross-section prediction of the $H^\pm e\nu_e$ final state.

If the collider energy does not allow for pair production and $\sqrt{s} > m_W + m_{H^\pm}$, the $W^\pm H^\mp$ production process can become the dominant source of charged Higgs bosons, depending on $\tan\beta$. In this case, as the process is loop-induced, the signal rate is much smaller than the typical pair-production rate. Even if H^+H^- production is the main production process at an e^+e^- collider, it would still be very rewarding to measure the $W^\pm H^\mp$ production cross section as well. While the H^+H^- cross section is determined at tree-level by the gauge couplings to photon and Z

---

[a] e-mail: oliver.brein@durham.ac.uk

boson, the $W^\pm H^\mp$ cross section is loop-induced and thus depends already at leading order on the virtual particles in the loops. Therefore, with a cross-section measurement of the latter process one would have access to information about the underlying model.

This paper presents a calculation of the MSSM prediction for the process $e^+e^- \to W^+H^-$. By the time the calculation this work is based on was finalised, another calculation of the same prediction appeared [19, 20]. We carried out a detailed comparison [25] of our results with those of [19, 20], which lead to agreement.[1] In the framework of THDM, the cross-section prediction for $e^+e^- \to W^+H^-$ is well known [21–23], and we could reproduce the results of [23] in particular.

In Sect. 2 we present the process $e^+e^- \to W^+H^-$ with the contributing Feynman diagrams in the MSSM and some details about our calculation. Section 3 presents our numerical results in two stages. In stage one, we examine the basic features of the $W^\pm H^\mp$ cross section for a 500 GeV and 1 TeV e^+e^- collider for two distinct MSSM parameter scenarios and compare the results also to predictions of a THDM with the same Higgs sector parameters. This enables us to exemplify the range of influence of virtual superpartners on the cross section. The effect of polarised electron and positron beams on the cross section is discussed briefly followed by a demonstration of the decoupling of superpartners with increasing supersymmetry-breaking scale. In stage two, we present results of a thorough scan of the MSSM parameter space for regions of large, possibly observable, cross section and try to understand for which parameter scenarios they arise. Section 4 contains our conclusions. Some results of this calculation were already reported in [24].

2 $e^+e^- \to W^+H^-$ in the MSSM

2.1 Kinematics

We study the reaction

$$e^+(\bar{k},\bar{\sigma}) + e^-(k,\sigma) \to W^+(p,\lambda) + H^-(\bar{p})\,,$$

where k and $\bar{k}$ denote the momenta of the initial-state electron and positron, p and $\bar{p}$ the momenta of the final-state gauge boson W^+ and Higgs boson H^-. Additionally, the electron, positron, and W boson are characterised by their spin polarisation $\sigma, \bar{\sigma}\ \left(= \pm\frac{1}{2}\right)$ and $\lambda (= 0, \pm 1)$. Neglecting the electron mass, the kinematical invariants $s = (k+\bar{k})^2$, $t = (k-p)^2$ and $u = (k-\bar{p})^2$ fulfill the relation

$$s + t + u = m_W^2 + m_{H^\pm}^2\,. \tag{1}$$

We assume unpolarised electron and positron beams. Thus, the differential cross section summed over spin polarisations of the final-state W boson reads

$$\frac{\mathrm{d}\sigma}{\mathrm{d}t} = \frac{1}{16\pi s^2} \sum_{\lambda=0,\pm1} \frac{1}{4} \sum_{\sigma,\bar{\sigma}=\pm\frac{1}{2}} \left|\mathcal{M}_{\sigma\bar{\sigma}\lambda}\right|^2 \tag{2}$$

with the helicity amplitudes $\mathcal{M}_{\sigma\bar{\sigma}\lambda}$ of the process. The total cross section is evaluated by numerical integration over the kinematically allowed t range:

$$\sigma_{e^+e^-\to W^+H^-}(s) = \int_{t_{\min}(s)}^{t_{\max}(s)} \mathrm{d}t\, \frac{\mathrm{d}\sigma}{\mathrm{d}t}(s,t)\,. \tag{3}$$

2.2 Feynman graphs

In the MSSM and THDM all leptons couple gauge-invariantly to one of the two Higgs doublets and therefore also to the physical Higgs bosons. Thus, there is a non-vanishing tree-level amplitude for the process under study. The Feynman graphs on tree-level consist of three graphs with s-channel exchange of neutral Higgs bosons (h^0, H^0 and A^0) and one with a t-channel exchange of a neutrino. The Yukawa couplings that appear in all tree-level graphs are $\propto m_e/m_W \approx 6\times10^{-6}$ and suppress the tree-level contribution strongly. The tree-level amplitude can thus safely be neglected and consequently there are no photon bremsstrahlung corrections at leading order.

In our calculation we take into account all one-loop contributions to the amplitude that do not vanish in the limit $m_e = 0$. For this reason, Feynman graphs with insertion of a s-channel Z–A mixing self-energy, or a t-channel neutrino self-energy, or radiative corrections to e^+e^- $\{h^0, H^0, A^0\}$ Yukawa couplings or to the $e^\pm\nu_e H^\mp$ Yukawa coupling need not be considered. There remain Feynman graphs with insertions of a W^-–H^- or G^-–H^- mixing self-energy at the external leg of the outgoing charged Higgs boson (see Fig. 1), graphs containing the loop-induced γW^+H^- and ZW^+H^- vertices,[2] box-type graphs (see Figs. 2 and 3) and the appropriate counterterm diagrams (see Fig. 4). The amplitude divides into Feynman graphs that contain either solely THDM particles (Fig. 1b,c, upper lines, and Fig. 2) or solely superpartners (Fig. 1b,c, lower lines, and Fig. 3) in the loop.

2.3 Calculation

Although the tree-level contribution vanishes in the limit of vanishing electron mass, which we consider, the need for renormalisation arises at one loop. There are diver-

---

[1] As a result, the formulae in [19, 20] are now checked by an independent calculation. According to [25] the results agree, if in (C14) of [19, 20] the tensor coefficient D_{23} in the coefficient of $\mathcal{A}_6 g_R^W g_H^L$ is replaced by $2D_{23}$. Furthermore, our comparison spotted two more errors in the numerical implementation of the results of [19, 20]. Before the corrections, the differential cross section at one phase space point for one particular MSSM parameter scenario calculated by the authors of [19, 20] was 12% below our result.

[2] Note that there is no tree-level $ZW^\pm H^\mp$ coupling in the MSSM or THDM [26].

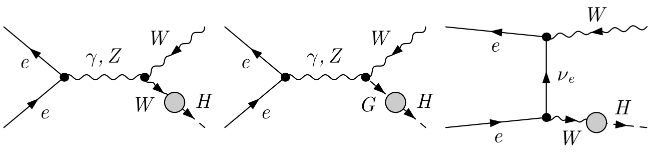

(a) graphs with self-energy insertions

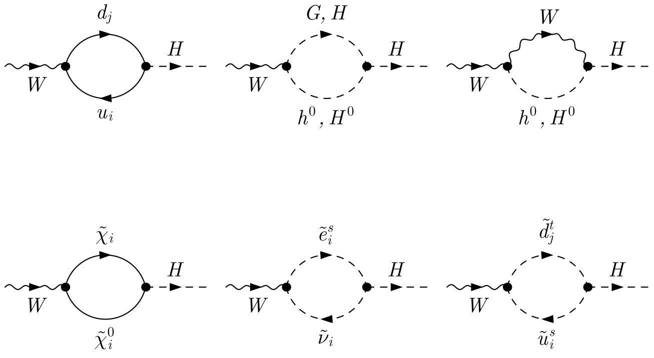

(b) W^+–H^- self-energy

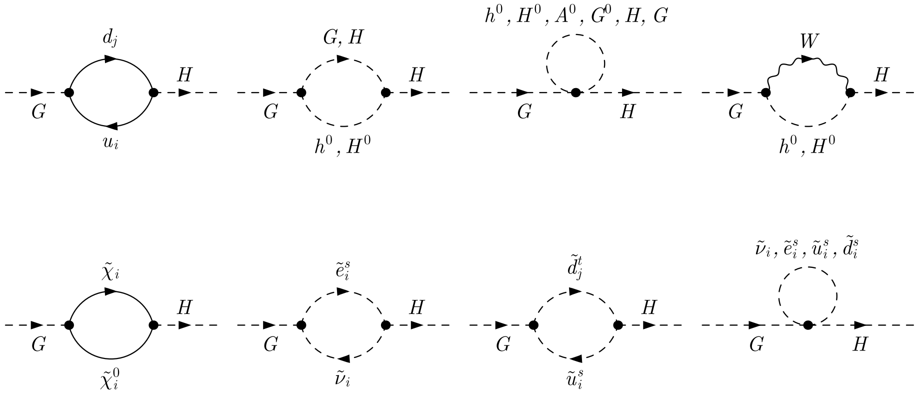

(c) G^+–H^- self-energy

Fig. 1. Feynman graphs for the process $e^+e^- \to W^+H^-$ with self-energy insertions. Each combination of particle labels corresponds to a separate Feynman graph

gent vector–scalar and scalar–scalar mixing propagators (Fig. 1) and vertex-type graphs (Figs. 2 and 3)[3]. We use the on-shell renormalisation scheme of [27–29], the application of which to $W^{\pm}$–$H^{\mp}$ self-energies is discussed in detail in [30]. In the MSSM no new types of divergent vertex functions occur. Merely, additional loop contributions with virtual superpartners add to the existing types of vertex functions. Therefore, we can take over the renormalisation conditions from [23] directly, which are briefly summarised in the following.

In order to generate the counter-terms, which are needed to renormalise the amplitude under study, it is sufficient to introduce field renormalisation constants for the MSSM Higgs doublets H_1 and H_2 and renormalisation constants for their vacuum expectation values v_1 and v_2:

$$H_i \to \sqrt{Z_{H_i}}H_i\,, \quad v_i \to \sqrt{Z_{H_i}}(v_i - \delta v_i)\,, \quad i = 1,2\,. \tag{4}$$

Expanding the renormalisation constants in the MSSM Lagrangian to one-loop order, $Z_{H_i} = 1 + \delta Z_{H_i}^{(1)}$ and $\delta v_i = \delta v_i^{(1)}$, generates the counter-term interactions needed and the corresponding Feynman rules:

$$\Gamma_{\mathrm{CT}}[H^{\mp}W^{\pm}(k^{\mu})] = \mathrm{i}\frac{k^{\mu}}{m_W}m_W^2\,\delta Z_{HW}\,, \tag{5}$$

$$\Gamma_{\mathrm{CT}}[\gamma_{\mu}W_{\nu}^{\pm}H^{\mp}] = -\mathrm{i}em_W g_{\mu\nu}\,\delta Z_{HW}\,, \tag{6}$$

$$\Gamma_{\mathrm{CT}}[Z_{\mu}W_{\nu}^{\pm}H^{\mp}] = \mathrm{i}em_W\frac{s_{\mathrm{W}}}{c_{\mathrm{W}}}g_{\mu\nu}\,\delta Z_{HW}\,, \tag{7}$$

with

$$\delta Z_{HW} = \sin\beta\cos\beta\left(\frac{\delta v_1}{v_1} - \frac{\delta v_2}{v_2} + \frac{\delta Z_{H_2} - \delta Z_{H_1}}{2}\right), \tag{8}$$

where $Z, W^{\pm}$ und γ denote the electroweak gauge bosons and the photon, and k^{μ} the momentum of the $W^{\pm}$ boson, chosen as incoming. In the on-shell scheme the following renormalisation conditions are posed.

---

[3] In principle, also divergent tadpole insertions appear, which we do not display, because we will choose a renormalisation condition such that those contributions vanish (see (9) and (10)).

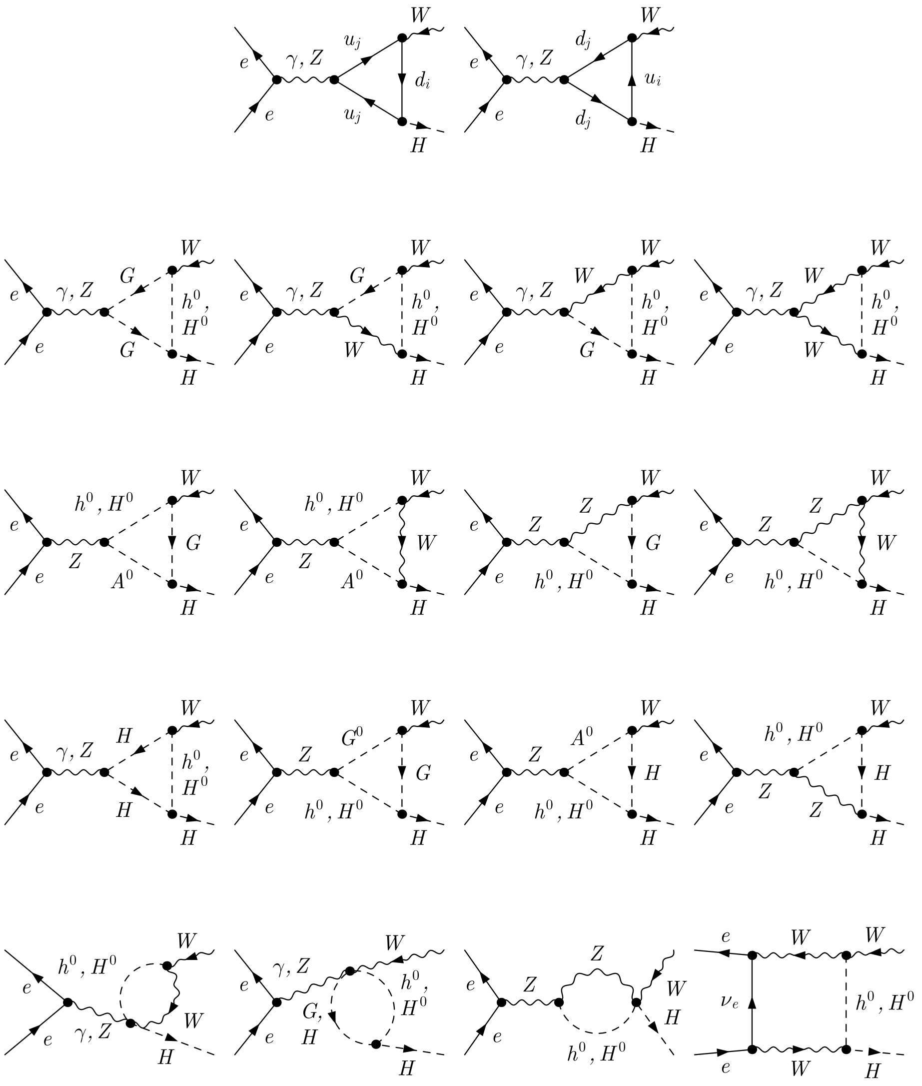

Fig. 2. The THDM subset of Feynman graphs of vertex and box type for the process $e^+e^- \to W^+H^-$. Each combination of particle labels corresponds to a separate Feynman graph

- Renormalised tadpole graphs vanish, i.e.

$$\hat{t}_{h^0} = t_{h^0} + \delta t_{h^0} = 0\,, \tag{9}$$

$$\hat{t}_{H^0} = t_{H^0} + \delta t_{H^0} = 0\,. \tag{10}$$

  This guarantees that the parameters v_1 and v_2 in the renormalised Lagrangian describe the minimum of the Higgs potential at one-loop order.
- Real charged Higgs bosons $H^{\pm}$ do not mix with longitudinally polarised $W^{\pm}$ bosons, i.e. the real part of the renormalised $H^{\pm}$–$W^{\mp}$ mixing self-energy,[4]

$$\hat{\varSigma}_{HW}(k^2) = \varSigma_{HW}(k^2) - m_W^2 \delta Z_{HW}\,, \tag{11}$$

  vanishes if the momentum k of $H^{\pm}$ is on mass-shell:

$$\operatorname{Re} \hat{\varSigma}_{HW}(k^2)\big|_{k^2 = m^2_{H^{\pm}}} = 0\,. \tag{12}$$

The condition (12) fixes the renormalisation constant δZ_{HW}:

$$\delta Z_{HW} = \frac{1}{m_W^2} \operatorname{Re} \varSigma_{HW}(m^2_{H^{\pm}})\,. \tag{13}$$

Because of the BRS symmetry of the renormalised Lagrangian the renormalisation of the divergent $H^{\pm}$–$G^{\mp}$ mixing self-energy is connected with the $H^{\pm}$–$W^{\mp}$ mixing self-energy through a Slavnov–Taylor identity [30]:

$$k^2 \hat{\varSigma}_{HW}(k^2) - m_W^2 \hat{\varSigma}_{HG}(k^2) = 0\,. \tag{14}$$

As a consequence, the real part of the renormalised $H^{\pm}$–$G^{\mp}$ mixing self-energy,

$$\hat{\varSigma}_{HG}(k^2) = \varSigma_{HG}(k^2) - k^2 \delta Z_{HG}\,, \tag{15}$$

also vanishes for $k^2 = m^2_{H^{\pm}}$:

$$\operatorname{Re} \hat{\varSigma}_{HG}(k^2)\big|_{k^2 = m^2_{H^{\pm}}} = 0\,. \tag{16}$$

---

[4] The renormalised $H^{\pm}$–$W^{\mp}$ mixing self-energy is defined as the coefficient of $-\mathrm{i}\frac{k^{\mu}}{m_W}$ of the amputated renormalised $H^{\pm}$–$W^{\mp}$ propagator.

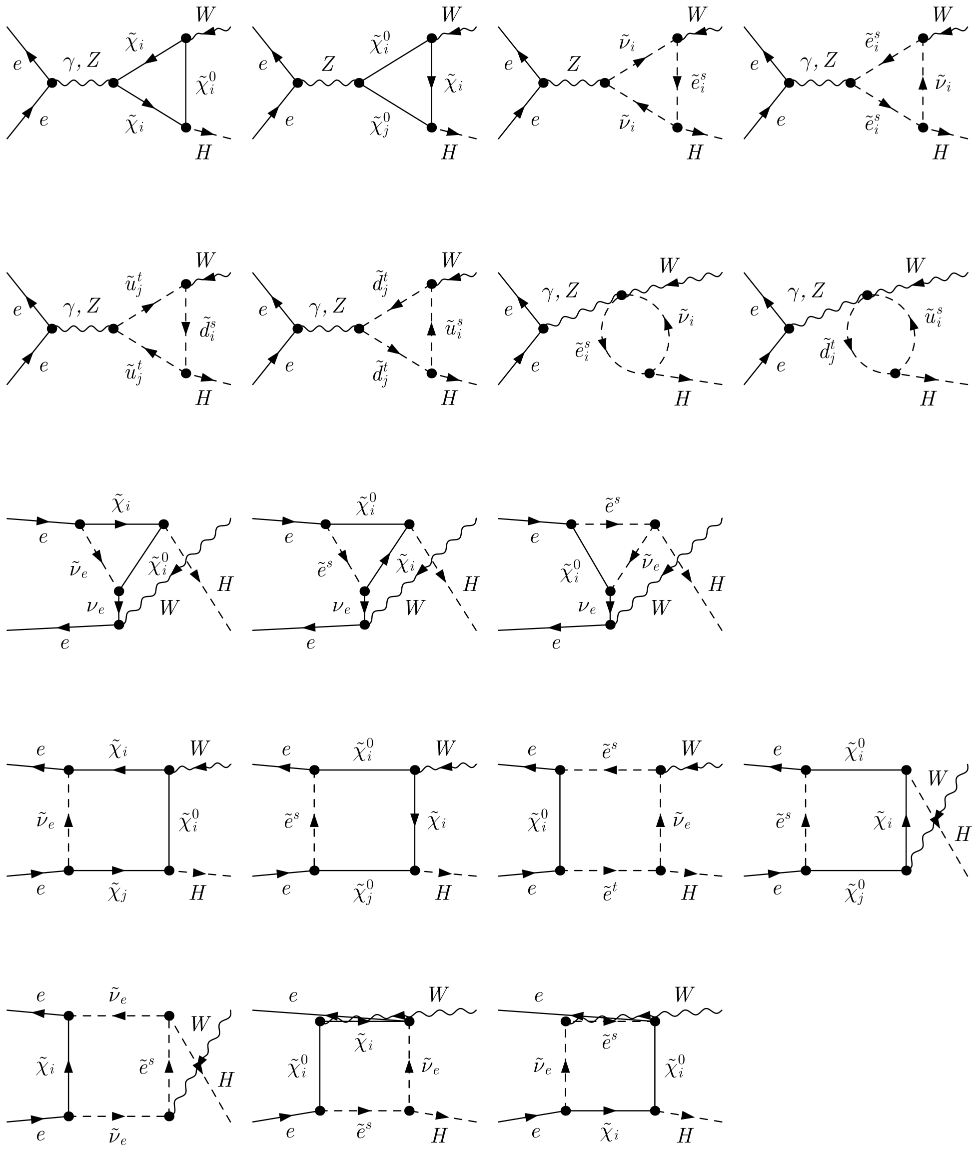

Fig. 3. The superpartner-loop subset of vertex and box type for the process $e^{+}e^{-} \to W^{+}H^{-}$. Each combination of particle labels corresponds to a separate Feynman graph

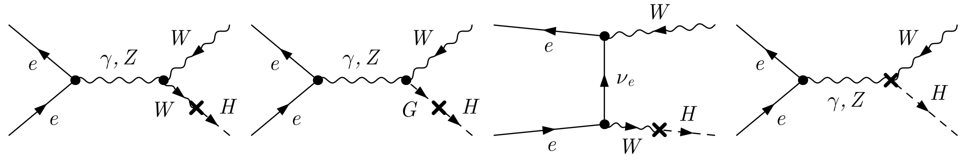

Fig. 4. Counter-term diagrams for $e^{+}e^{-} \to W^{+}H^{-}$

The Feynman rule for the corresponding counter-term interaction thus reads:

$$\Gamma_{\mathrm{CT}}[H^{\mp}G^{\pm}(k)] = \mathrm{i}k^2 \delta Z_{HG} \qquad (17)$$

with $\delta Z_{HG} = -\operatorname{Re} \Sigma_{HG}(m^2_{H^{\pm}})/m^2_{H^{\pm}}$.

The calculation of the amplitude has been performed in 't Hooft–Feynman gauge using constrained differential renormalisation [31, 32] with the help of the computer programs FeynArts and FormCalc [33–37]. To that end, the counter-term definitions and Feynman rules of counter-term interactions that were needed were added to the MSSM model file for FeynArts.

3 Results

There are two major motivations for studying the MSSM prediction for $e^{+}e^{-} \to W^{\pm}H^{\mp}$ cross sections at the international linear collider (ILC). Firstly, it is important to know the expected event rates at the ILC either to confirm the discovery of charged Higgs bosons at the LHC or to assess the $H^{\pm}$ discovery potential of the ILC beyond the pair-production limit of $\sqrt{s}/2$. Secondly, the observation of this process provides the opportunity to glean some information about the underlying model because of its potential sensitivity to virtual superpartners.

The predictions for $W^\pm H^\mp$ production in the framework of the general THDM are well known [21–23]. Our concern is to demonstrate possible distinctive differences between the MSSM and the THDM. To that end, we compare the prediction of our complete one-loop calculation in the MSSM with the THDM prediction with the Higgs sector parameters restricted to MSSM values (sTHDM). The latter model corresponds to the MSSM with decoupled superpartners. Thus, one achieves insight in the contribution of superpartner loop-graphs to the cross section.

3.1 MSSM parameter restrictions

The MSSM parameter space is constrained by unsuccessful searches for Higgs bosons and supersymmetric partners and other measurements, the theoretical predictions of which are sensitive to supersymmetric contributions. We try to take into account major constraints on the MSSM parameter space. Specifically, we take into account four types of constraints.

Higgs search at LEP: we calculate for each parameter point the MSSM predictions for m_{h^0} and $\sigma(e^+e^- \to h^0 Z) \times \mathrm{BR}(h^0 \to b\bar{b})$ and exclude it if the m_{h^0}-dependent LEP bound on $\sigma \times \mathrm{BR}$ is violated (according to Table 14(b) of [38]). We use FeynHiggs 2.5.1 [39–42] for calculating the m_{h^0} prediction and allow for a theoretical uncertainty of 3 GeV.

$b \to s\gamma$: we calculate the leading-order MSSM prediction for the branching ratio $\mathrm{BR}(B \to X_s \gamma)$ [43, 44][5] and exclude parameter points if the prediction falls outside of the range $(3.55 \pm 1.71) \times 10^{-4}$. This range is determined by using the experimental central value [46–48] and adding up the experimental 3σ interval ($\approx 10^{-4}$) and an estimate of the independent theoretical uncertainty (0.71×10^{-4}). The latter estimate (20%) is guided by the discussion of theoretical uncertainties for the SM prediction [50]. Overall, the acceptance range is generous enough to accommodate also the neglected large radiative corrections to the branching ratio for large $\tan\beta$ as an additional theoretical uncertainty.

Electroweak ρ-parameter: we take care that the dominant squark contribution to the electroweak ρ-parameter [49] stays below 0.0025 [51].

Direct searches for superpartners: parameter points have to be consistent with the following exclusion limits [51]:

$$m_{\tilde{t}_i} \geqslant 95.7\,\mathrm{GeV}\,, \quad m_{\tilde{b}_i} \geqslant 89\,\mathrm{GeV}\,, \quad m_{\tilde{q}\neq\tilde{b},\tilde{t}} \geqslant 150\,\mathrm{GeV}\,,$$
$$m_{\tilde{\chi}^0} \geqslant 46\,\mathrm{GeV}\,, \quad m_{\tilde{\chi}^\pm} \geqslant 94\,\mathrm{GeV}\,, \quad M_{\tilde{\ell}} \geqslant 73\,\mathrm{GeV}\,.$$

We do not take into account the constraints on the MSSM parameters resulting from the measurement of the anomalous magnetic moment of the muon a_μ [52–54]. In order to keep our exemplary study simple, we choose to have only one common sfermion mass scale $M_{\tilde{f}}$. Certain scenarios might lead to MSSM predictions for a_μ that are incompatible with the measurement but would not be if the first two generations of sfermions had a different mass scale than the third. Yet, in the process studied here, among the sfermions only the third-generation ones, especially the squarks, are important. Furthermore, as it turns out, in areas where the $W^\pm H^\mp$ production cross section is large, the gaugino mass parameters are of minor importance. Therefore, we disregard the a_μ-constraint here, because for a given parameter scenario, which is in conflict with it, there will usually exist a rearrangement of parameter values that meets the constraint but changes the process under study in the areas of interest only insignificantly.[6]

3.2 Cross section for specific parameter scenarios

In order to demonstrate possible differences between the sTHDM and the full MSSM, we are interested in scenarios that potentially show large effects from virtual superpartners. It turns out that the MSSM benchmark scenarios for the neutral Higgs search at LEP [59], which have been slightly modified in [38], also make good sample scenarios for the charged Higgs production process studied here. We pick two scenarios from [38]: the $m_h^{\max}$ scenario with a lower sfermion mass scale and the small-α_{eff} scenario. The two MSSM parameter scenarios are specified as follows.

$m_h^{\max}(400)$ *scenario:* the soft-breaking sfermion mass parameter is set to $M_{\tilde{f}} = 400\,\mathrm{GeV}$. The off-diagonal term X_t $(= A_t - \mu\cot\beta)$ in the top-squark mass matrix is set to $2M_{\tilde{f}}$ $(= 800\,\mathrm{GeV})$ The Higgsino and gaugino mass parameters have the settings $\mu = -200\,\mathrm{GeV}$, $M_1 = M_2 = 200\,\mathrm{GeV}$, $M_{\tilde{g}} = 800\,\mathrm{GeV}$. When $\tan\beta$ is changed, A_t is changed accordingly to ensure $X_t = 2M_{\tilde{f}}$. The settings of the other soft-breaking scalar-quark Higgs couplings are $A_b = A_t$ and $A_f = 0$ $(f = e, \mu, \tau, u, d, c, s)$.

Small-α_{eff} scenario: this scenario gives rise to suppressed branching ratios for the decays $h^0 \to b\bar{b}$ and $\tau^+\tau^-$, especially for large $\tan\beta$ and moderate values of m_A. The settings are: $M_{\tilde{f}} = 800\,\mathrm{GeV}$, $X_t = -1100\,\mathrm{GeV}$, $M_1 = M_2 = 500\,\mathrm{GeV}$ and $\mu = 2000\,\mathrm{GeV}$. Also, here A_t is changed if $\tan\beta$ changes in order to keep the value of X_t fixed, $A_b = A_t$ and $A_f = 0$ $(f = e, \mu, \tau, u, d, c, s)$.

We present results for two collider energies, $\sqrt{s} = 500\,\mathrm{GeV}$ and 1000 GeV. Assuming the collider would accumulate 1000 events/fb of integrated luminosity, a cross section of 0.05 fb would result in 50 expected events, which we take here as a reasonable lower limit for the observability of this charged Higgs production channel. For a 500 GeV machine, the currently envisaged running schedule will actually only result in 500 events/fb after four years of running.

3.2.1 Results for the $m_h^{\max}(400)$ scenario

In Figs. 5a and 6a the $e^+e^- \to W^\pm H^\mp$ cross sections for a collider energy of 500 GeV are displayed for the full MSSM and the corresponding sTHDM. Figure 5a shows

---

[5] The code we are using is taken from [45].

[6] Using the results of [55–58] we convinced ourselves that this is indeed the case by examining a large set of sample scenarios.

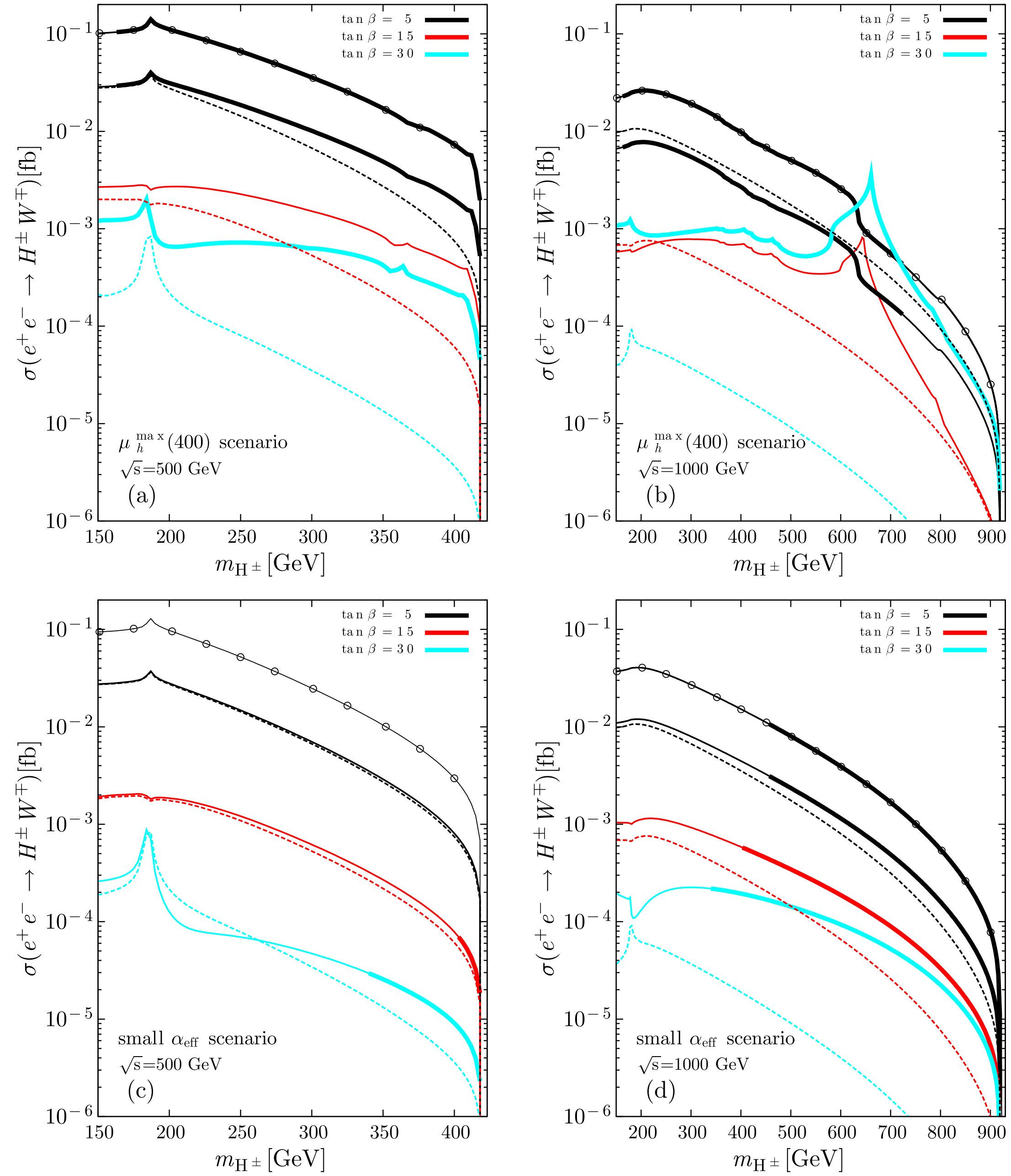

Fig. 5. Unpolarised cross section $\sigma(e^+e^- \to H^\pm W^\mp)$ versus $m_{H^\pm}$ for different values of $\tan\beta$ for the $m_h^{\max}(400)$ and small-$\alpha_{\rm eff}$ scenarios (*solid lines*) and the corresponding sTHDM scenario (*dashed lines*) for $\sqrt{s} = 500$ GeV and $\sqrt{s} = 1000$ GeV. *Thick solid lines* indicate consistency of the MSSM scenarios with parameter restrictions. The cross section for optimal polarisation is shown for $\tan\beta = 5$ (*solid lines* with *circles*)

the $m_{H^\pm}$-dependence for $\tan\beta = 5$, 15, and 30. The spike in all predictions for $m_{H^\pm} \equiv \sqrt{\bar{p}^2} \approx 180$ GeV $\approx m_t + m_b$ is due to a threshold effect in the vertex graphs with virtual top- and bottom-quarks (see Fig. 2). Similar threshold effects are seen in the full MSSM prediction where $m_{H^\pm}$ is just at a threshold of the superpartner loop-amplitudes. For instance, the cusps in the MSSM predictions above 350 GeV in Fig. 5 a are all due to chargino–neutralino thresholds, where $m_{H^\pm} \approx m_{\chi_i^0} + m_{\chi_j^+}$.

Figure 6a shows the $\tan\beta$-dependence for $m_{H^\pm} =$ 190 GeV, 250 GeV, and 350 GeV. Note that for each value of $m_{H^\pm}$ a separate range of high and low $\tan\beta$ is consistent with MSSM parameter restrictions. The excluded areas are in conflict with the constraint from BR$(B \to X_s\gamma)$: the BR is too low for intermediate $\tan\beta$ and too high for very small or very large $\tan\beta$. For large values of $\tan\beta$, the MSSM cross section is generally much larger than in the sTHDM. For instance, for $m_{H^\pm} = 350$ GeV in the allowed high-$\tan\beta$ range the MSSM prediction exceeds the sTHDM prediction about 50-fold. Unfortunately, even this cross section is not large enough to lead to an observable production rate if 1000 events/fb of integrated luminosity are assumed.

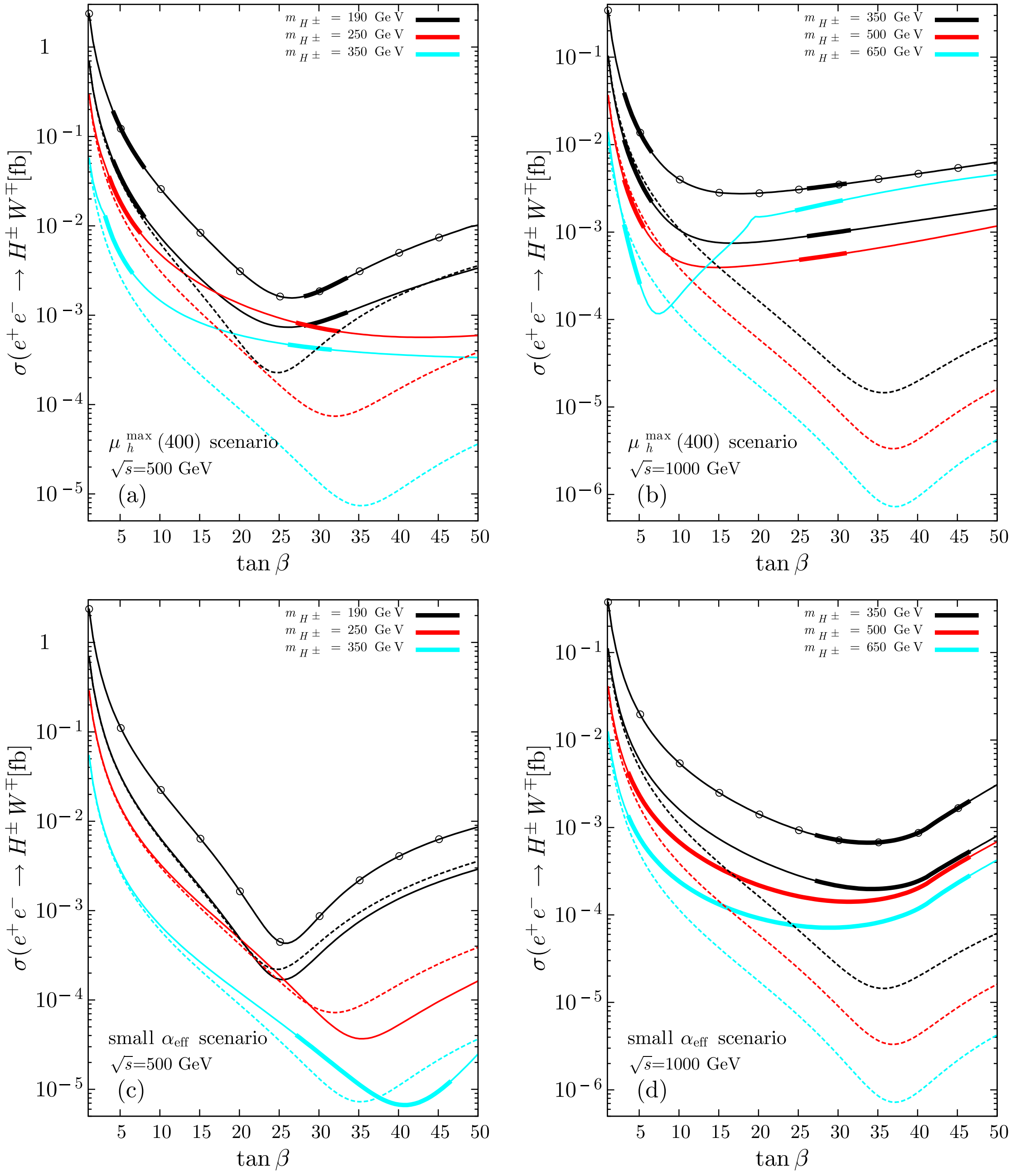

Fig. 6. Unpolarised cross section $\sigma(e^+e^- \to H^\pm W^\mp)$ versus $\tan\beta$ for different values of $m_{\rm H^\pm}$ for the $m_h^{\rm max}(400)$ and small-$\alpha_{\rm eff}$ scenarios (*solid lines*) and the corresponding sTHDM scenario (*dashed lines*) for $\sqrt{s} = 500$ GeV and $\sqrt{s} = 1000$ GeV. *Thick solid lines* indicate consistency of the MSSM scenarios with parameter restrictions. The cross section for optimal polarisation is shown in each panel for one value of $m_{\rm H^\pm}$ (*solid lines* with *circles*)

For $\sqrt{s} = 1000$ GeV Figs. 5b and 6b reveal the same general behaviour. Yet, due to the higher collider energy, more superpartner thresholds are within the accessible mass range for the charged Higgs boson. Most notably, the sharp rise and fall of the cross section between 550 GeV and 700 GeV are due to $\tilde{t}_1$–$\tilde{b}_1$ and $\tilde{t}_1$–$\tilde{b}_2$ thresholds. For $\tan\beta = 5$, $m_{\tilde{b}_1}$ and $m_{\tilde{b}_2}$ lie so close to each other that only a sharp dip occurs at $m_{H^\pm} \approx m_{\tilde{t}_1} + m_{\tilde{b}_{1,2}}$. In Fig. 6b the edge in the $\tan\beta$-dependence of the MSSM cross section for $m_{H^\pm} = 650 GeV$ is also due to the $\tilde{t}_1$–$\tilde{b}_2$ threshold: the value of $m_{\tilde{t}_1} + m_{\tilde{b}_2}$ rises with $\tan\beta$ and crosses 650 GeV just around $\tan\beta = 20$.

For $\tan\beta = 15$ this MSSM scenario is ruled out for all values of $m_{H^\pm}$ considered here, because the resulting BR($B \to X_s\gamma$) is too low (of the order of 10^{-5}).

3.2.2 Results for the small-$\alpha_{\rm eff}$ scenario

In contrast to the previous scenario all superpartner thresholds are beyond reach even at $\sqrt{s} = 1$ TeV in the

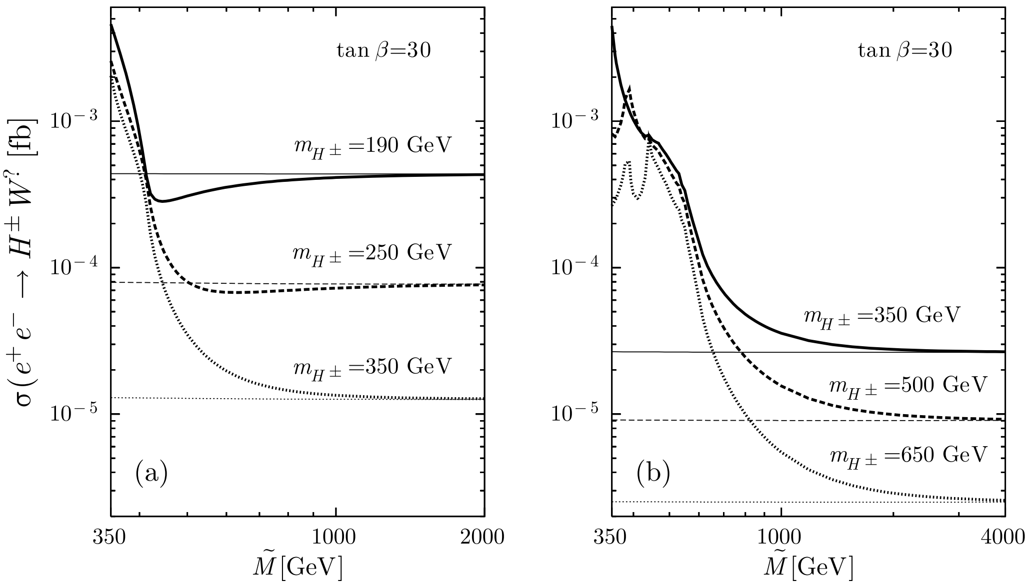

Fig. 7. Cross section for the process $e^+e^- \to H^\pm W^\mp$ as a function of a common superpartner mass scale $\widetilde{M}$ for a **a** 500 GeV and **b** 1 TeV e^+e^- collider

small-α_{eff} scenario. The lowest chargino–neutralino threshold is at about 1 TeV and the lowest stop–sbottom threshold above about 1.1 TeV depending on $\tan\beta$. The Feynman graphs with virtual squarks of the third generation dominate the superpartner contributions to the scattering amplitude. For large $\tan\beta$ they are even the dominant contribution to the cross section. This scenario has significant mixing in the stop sector. Thus, potentially large terms in the couplings of third-generation squarks to Higgs bosons[7] are weighted by a factor of order 1, especially the terms proportional to $m_t\mu$ and $m_b A_b \tan\beta$.

Figures 5c and 6c show the predicted cross section for a 500 GeV collider and Figs. 5d and 6d for a 1 TeV collider. The interference between Feynman graphs with virtual THDM particles and superpartners is always constructive for $\sqrt{s} = 1$ TeV. Especially for large $\tan\beta$ the MSSM cross section can be enhanced by up to two orders of magnitude (see Fig. 6d). For $\sqrt{s} = 500$ GeV also destructive interference is possible. In this case, the strongest suppression factor for the MSSM cross section with respect to the sTHDM we get in our sample cases is about 1/3.

3.2.3 Effect of polarised electrons and positrons

The cross section of $e^+e^- \to W^\pm H^\mp$ depends strongly on the polarisation of the incoming electrons and positrons. Specifically, the cross section varies roughly by one order of magnitude between the optimal situation where all electrons have helicity -1 and all positrons have helicity $+1$, i.e. $P(e^-) = -1$ and $P(e^+) = +1$, and the opposite situation where $P(e^-) = +1$ and $P(e^+) = -1$.

In order to illustrate the effect of polarised beams at the ILC, we include in Figs. 5a to d the cross-section prediction for optimal polarisation for $\tan\beta = 5$. Likewise, we include in Fig. 6a,c and b,d the cross-section prediction for optimal polarisation for $m_{H^\pm} = 190$ GeV and 350 GeV, respectively. Optimal polarisation leads to an increase in cross section varying between a factor of 2 up to 3.8 depending on $m_{H^\pm}$ and $\tan\beta$ for both collider energies.

3.2.4 Decoupling of superpartners

We set all soft-breaking parameters that appear in our expression for the MSSM cross section equal to a single supersymmetry-breaking scale $\widetilde{M}$,

$$\widetilde{M} = M_{\tilde{f}} = A_b = A_t = M_1 = M_2 = \mu\,, \qquad (18)$$

and study the behaviour of the MSSM cross section with rising $\widetilde{M}$ compared to the sTHDM prediction. This allows us to demonstrate the decoupling of the virtual superpartner contributions to the cross section.

Figure 7a shows results for a 500 GeV collider and $m_{H^\pm} = 190$, 250, and 350 GeV with $\widetilde{M}$ varied between 350 and 2000 GeV. The MSSM results drop significantly once all superpartners get heavy enough for threshold effects to disappear. A similar behaviour is shown in Fig. 7b for a 1000 GeV collider and $m_{H^\pm} = 350$, 500, and 650 GeV where $\widetilde{M}$ is varied up to 4 TeV. Notably, even at a soft-breaking scale of 1 TeV, the MSSM surpasses the sTHDM prediction by a factor of 1.4, 1.7, and 2.2 for these three mass values, respectively.

3.3 Parameter scan

We have already demonstrated the possibility of strong enhancement of the MSSM cross-section prediction by virtual superpartner effects. This raises the question of whether there exist regions where $W^\pm H^\mp$ production could be observable in the MSSM but not in the sTHDM. We investigate this more systematically by scanning over the relevant MSSM parameter space.

---

[7] A list of the relevant couplings in our notation can be found in [60, 61].

The detectors at the LHC will be capable of finding an MSSM charged Higgs boson only in certain regions in the m_{A^0}–$\tan\beta$ plane. Likewise, the ILC can detect charged Higgs bosons easily only if pair production is kinematically possible. Thus, $W^{\pm}H^{\mp}$ production at the ILC either may allow for an independent confirmation of a previous discovery or it can be a discovery process. In the first case, it makes sense to combine the knowledge of the mass of the charged Higgs boson with the knowledge of the cross-section prediction in the MSSM and adjust the collider energy to the maximum of the expected cross section as a function of $\sqrt{s}$. In the second case, it is difficult to say what the best strategy of choosing $\sqrt{s}$ will be for searching for the charged Higgs boson. A reasonable assumption is however that a significant fraction of the data during ILC operation will be collected at the highest collider energy.

With these two possibilities in mind, we perform two parameter scans. Scan 1 assumes that the charged Higgs mass and $\tan\beta$ is known and that it makes sense to adjust the collider energy to maximise the cross section.[8] We thus fix $m_{H^{\pm}}$ and $\tan\beta$ in our scan and include $\sqrt{s}$ in the list of scanned parameters. Scan 2 fixes $\sqrt{s}$ at the maximal collider energy but includes $m_{H^{\pm}}$ and $\tan\beta$ in the list of scanned parameters. For both scans we assume an ILC with a maximal collision energy of 1 TeV and that the charged Higgs boson cannot be pair produced.

In general, we are interested in regions of parameter space where the cross section is large, such that the process may be detectable at the ILC, i.e. cross sections above say 0.05 fb, which would lead to more than 50 events if $1000\,\mathrm{fb}^{-1}$ of integrated luminosity is assumed. The parameter spaces we scan over are six to seven dimensional. For a good coverage of the interesting region in such many-dimensional parameter spaces, scanning over a fixed grid of points or naively sampling random points is not very effective. In order to increase the number of scanned parameter points in the region of large cross section, we use the "adaptive scanning" algorithm described in more detail in [62]. This means essentially that we are using the importance sampling algorithm VEGAS [63, 64] to evaluate the integral of the cross section over the relevant MSSM parameters. We are not interested in the value of the integral as such but store the sampled points that automatically accumulate in the region of large cross section. More precisely, the quantity we are integrating over in our scans is identical to the cross section only at 'allowed' points according to the parameter restrictions described in Sect. 3.1, and zero otherwise. The accumulation of points thus also focuses on the allowed region. In all scans we only keep sampled parameter points that fulfill all the constraints described in Sect. 3.1.

Before presenting the results of our scans, we have to discuss one critical issue[9]. Threshold effects are an important mechanism of enhancement for the cross section we study here and our scanning procedure samples regions of parameter space where such effects are important more thoroughly. However, it is known that the evaluation of loop-amplitudes near thresholds becomes inaccurate if the unstable virtual particles are approximated as stable ones, i.e. neglecting their widths. In our calculation we use this approximation, which might lead to an overestimation of the cross section near thresholds.

In a previous project [61] the numerical effect of introducing the widths of virtual particles in similar loop-integrals on the values of those integrals and the resulting cross section have been studied. For typical squark widths of up to 1 GeV the effect on the cross section was a reduction by up to 10% in a small vicinity of the threshold region (less than ±10% around the threshold).

We investigated how important the nearness to thresholds is for the cross section values in our scans. We find that the only relevant threshold in the large cross-section region is the stop–sbottom threshold, where $m_{H^{\pm}} = m_{\tilde{t}_1} + m_{\tilde{b}_1}$. Indeed, we get the highest cross sections distributed around $x := (m_{\tilde{t}_1} + m_{\tilde{b}_1})/m_{H^{\pm}} = 1$. In order to assess whether a possible overestimation introduced by our approximation has distorted our results we did the following check. We regenerated Figs. 8 to 10 reducing the cross section σ by 50% if $|x| < 10\%$ and leaving it untouched otherwise. A reduction of σ in the threshold region by 50% is of course much more than was found in [61]. With this prescription, the only visible change is the absence of the orange points and a slight depletion of the light blue points in Figs. 8 and 10.

3.3.1 Scan 1: $m_{H^{\pm}}$ and $\tan\beta$ known

The MSSM input parameters are scanned over the following region:

$$\begin{aligned} M_{\tilde{f}}, M_1, M_2 &= 10\ldots2000\,\mathrm{GeV}\,, \\ \mu, A_t, A_b &= -4000\ldots4000\,\mathrm{GeV}\,, \\ \sqrt{s} &= 500\ldots1000\,\mathrm{GeV}\,, \\ m_{H^{\pm}} &= 500\,\mathrm{GeV}\,, \\ \tan\beta &= 3,\ 15,\ 30\,. \end{aligned} \tag{19}$$

The $\tan\beta$ values respectively lie roughly at the lower, middle, and upper end of the wedge region. The less influential parameters are set to $M_{\tilde{g}} = 800\,\mathrm{GeV}$ and $A_f = 0$ ($f = e, \mu, \tau, u, d, c, s$). Examining the results by studying projections of the cross section on all one- and two-dimensional subspaces of the scanned parameter space we find that the gaugino mass parameters M_1 and M_2 have negligible influence for cross sections down to 10^{-3} fb. We also study the dependence of the cross section on the squark mixing parameters X_t, X_b normalised to the sfermion mass scale $M_{\tilde{f}}$, i.e. $\hat{X}_t = (A_t - \mu/\tan\beta)/M_{\tilde{f}}$ and $\hat{X}_b = (A_b - \mu\tan\beta)/M_{\tilde{f}}$. In Fig. 8 we show the most interesting two-dimensional projections[10]. Note that in Figs. 8 and 10 parameter points with an "observable" cross section (above 0.05 fb) contain all blue and orange points and a subset of the yellow points.

---

[8] Judging from our present knowledge, it seems unrealistic that such an adjustment will be made.

[9] We thank the referee for raising this issue.

[10] The complete results of the parameter scans can be obtained via the following URL in [65].

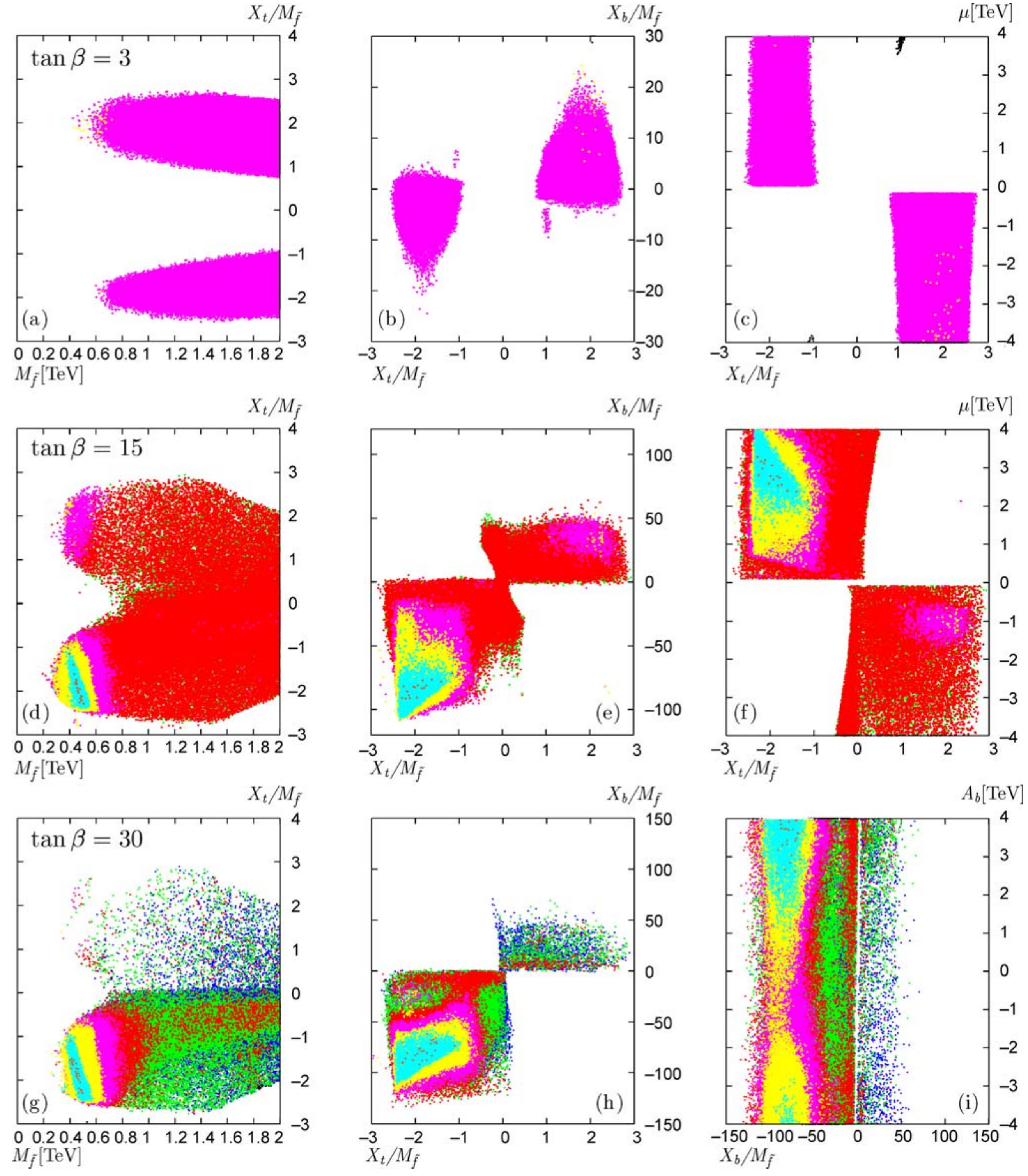

Fig. 8. Two-dimensional slices through the scanned parameter space of scan 1 for $\tan\beta = 3, 15$ and 30. The colours refer to bins of cross-section values: *orange*: $10\,\text{fb} \geq \sigma > 1\,\text{fb}$, *light blue*: $1\,\text{fb} \geq \sigma > 10^{-1}\,\text{fb}$, *yellow*: $10^{-1}\,\text{fb} \geq \sigma > 10^{-2}\,\text{fb}$, *cyan*: $10^{-2}\,\text{fb} \geq \sigma > 10^{-3}\,\text{fb}$, *red*: $10^{-3}\,\text{fb} \geq \sigma > 10^{-4}\,\text{fb}$, *green*: $10^{-4}\,\text{fb} \geq \sigma > 10^{-5}\,\text{fb}$, *blue*: $\sigma < 10^{-5}\,\text{fb}$. Points with larger values of σ are plotted on top of points with smaller values. Please refer to the on-line version for colours

For $\tan\beta = 3$ the most noticeable feature, shown in Fig. 8a–c, is that the highest values for the $H^{\pm}W^{\mp}$ production cross section lie typically between 10^{-3} fb and 10^{-2} fb and are reached everywhere in the allowed parameter region. In our scan we find a few cases with higher cross section, clearly visible as the scattered yellow dots on a cyan background. Yet, we find no scenario with a cross section above 0.1 fb. The well-known fact that

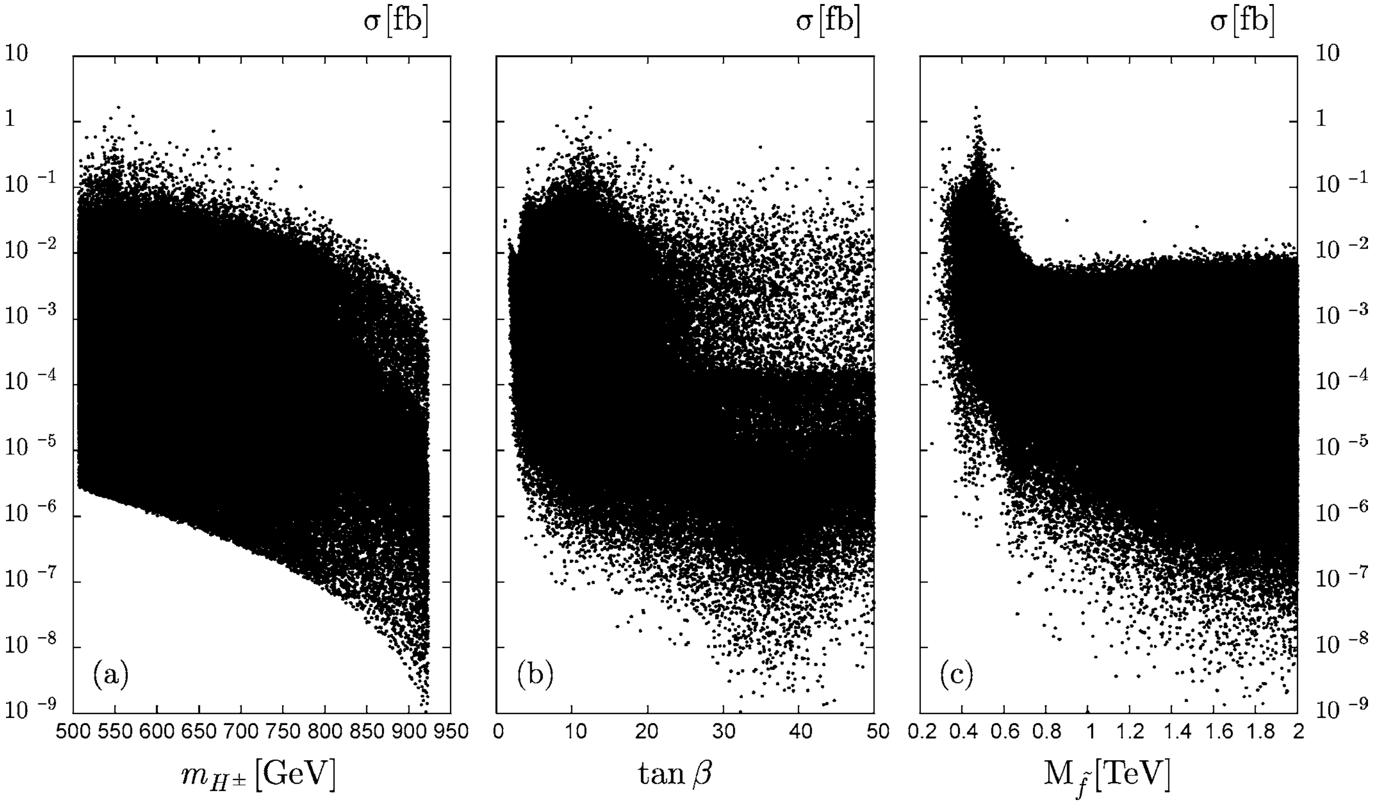

Fig. 9. Cross-section results of scan 2 versus **a** $m_{\mathrm{H}^\pm}$, **b** $\tan\beta$ and **c** $M_{\tilde f}$

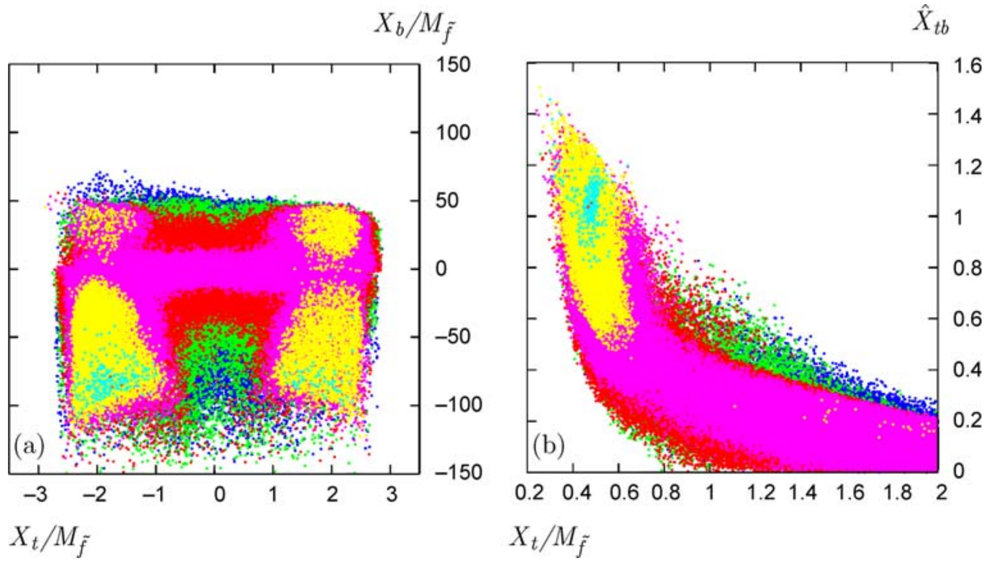

Fig. 10. Two-dimensional slices through the scanned parameter space of scan 2. The quantity $\hat X_{tb}$ in panel **b** is defined in (21). The colours refer to bins of cross-section values in the same way as in Fig. 8. Points with larger values of σ are plotted on top of points with smaller values. Please refer to the on-line version for colours

for small $\tan\beta$ the constraints, especially the LEP Higgs-mass bound, require a fair amount of stop mixing (i.e. $|\hat X_t| \gtrsim 1$) to be present, is clearly seen in all three figures.

Also owing to the LEP bound, the lowest common squark mass scale $M_{\tilde f}$ for which we find allowed scenarios is about 400 GeV for positive $\hat X_t$ and 600 GeV for negative $\hat X_t$. It is for rather low $M_{\tilde f}$, below about 650 GeV, that the few scenarios with a cross section above 10^{-2} fb appear. It turns out that having $M_{\tilde f} \lesssim 650$ GeV is a rather generic necessary requirement for scenarios with cross sections above 10^{-2} fb, as will become more clear in the following.

The projection on the $\hat X_t$–μ plane (Fig. 8c) reveals that almost all of the scenarios we find in our scan show a strict correlation between the sign of $\hat X_t$ and the sign of μ, the former being positive if the latter is negative and vice versa. This behaviour is due to the BR($B \to X_s\gamma$) constraint. For $m_{H^\pm} = 500$ GeV the branching ratio quickly saturates its upper bound if the product $\hat X_t\mu$ rises to positive values almost independently of the values of the other scanned parameters, except for a small region around $\hat{X}_t\mu = 4\,\text{TeV}$. This region can be seen in the upper right and lower left quarter of Fig. 8c. This near-perfect correlation between the signs of $\hat{X}_t$ and μ, and a similar correlation between the signs of $\hat{X}_t$ and $\hat{X}_b$, also holds for $\tan\beta = 15$ and 30 for the same reason (see Fig. 8e,f and h). However, for higher values of $m_{H^\pm}$ (say 800 GeV) this is not the case.

For $\tan\beta = 15$ (Fig. 8d,e and f) the results of the scan change drastically compared to the $\tan\beta = 3$ case. Firstly, the allowed region in the $M_{\tilde{f}}$–$\hat{X}_t$ plane (see Fig. 8d) is much larger, now also including scenarios without stop mixing and scenarios with $M_{\tilde{f}}$ below 300 GeV. Secondly, the highest cross-section values are considerably larger, of the order of 10 fb. The projection of the parameter points on the $M_{\tilde{f}}$–$\hat{X}_t$ plane (Fig. 8d) shows that the scenarios with a (large) cross section above 0.1 fb are confined to a very specific region with $M_{\tilde{f}}$ between 250 GeV and 600 GeV, and $\hat{X}_t$ between -2.5 and -1 simultaneously. It is only in this region that $m_{\tilde{t}_1} + m_{\tilde{b}_1}$ can be of the order of $m_{H^\pm}$ such that stop–sbottom loop-graphs can lead to enhancement of the cross section due to threshold effects.

The projection on the $\hat{X}_t$–$\hat{X}_b$ plane (Fig. 8e) shows that all large cross-section scenarios also have a significantly nonzero and negative value of $\hat{X}_b$. Quantitatively, it turns out that those scenarios typically have the two mass scales $m_t\hat{X}_t$ and $m_b\hat{X}_b$ of the same order of magnitude. Furthermore, from the projection on the $\hat{X}_t$–μ plane (Fig. 8f) we see that those scenarios also have a positive and large value of μ, typically between 2 TeV and the limit of our scan range (4 TeV). Looking into the $\hat{X}_b$-A_b plane (not depicted) we find large cross-section scenarios for almost any value of A_b.

The scan results for $\tan\beta = 30$ (Fig. 8g,h and i) look very similar to the previous case. Again, in order to obtain a cross section above 0.1 fb it appears that one needs a low sfermion mass scale $M_{\tilde{f}}$ between roughly 250 GeV and 600 GeV and a significant amount of mixing in the stop *and* sbottom sector with both $\hat{X}_t$ and $\hat{X}_b$ negative. One important change compared to the previous case is that all large cross-section scenarios have a rather large value of $|A_b| \gtrsim 1$ TeV (see Fig. 8i).

3.3.2 Scan 2: $m_{H^\pm}$ and $\tan\beta$ unknown

The MSSM input parameters are scanned over the following region:

$$\begin{aligned} M_{\tilde{f}} &= 10\ldots2000\,\text{GeV}\,, \\ \mu, A_t, A_b &= -4000\ldots4000\,\text{GeV}\,, \\ m_{H^\pm} &= 500\ldots920\,\text{GeV}\,, \\ \tan\beta &= 1\ldots50\,, \\ M_1 = M_2 &= 500\,\text{GeV}\,, \\ \sqrt{s} &= 1\,\text{TeV}\,. \end{aligned} \tag{20}$$

The less influential gaugino mass parameters M_1 and M_2 are fixed in order to obtain a more thorough scan over the relevant MSSM parameters. Furthermore, $M_{\tilde{g}}$ and $A_f (f \neq t, b)$ are chosen as in can 1.

Figure 9a shows the obtained cross-section values projected on the $m_{H^\pm}$-axis. Overall, the values drop with rising $m_{H^\pm}$ due to decreasing phase space. There are no scenarios with $\sigma > 0.1$ fb for $m_{H^\pm} \gtrsim 750$ GeV and no scenarios with $\sigma > 0.01$ fb for $m_{H^\pm} \gtrsim 875$ GeV. The projection on the $\tan\beta$-axis in Fig. 9b shows that there exist allowed parameter scenarios with cross sections even above 0.1 fb over the whole scanned range. Figure 9c shows the very distinct dependence of the cross section on the common sfermion mass scale $M_{\tilde{f}}$, which survives even after the inclusion of $m_{H^\pm}$ and $\tan\beta$ in the scan. Evidently, cross sections significantly above 0.1 fb are only possible if 275 GeV $\lesssim M_{\tilde{f}} \lesssim$ 700 GeV where threshold enhancement in stop–sbottom loop-graphs occurs. A detection of squarks with masses in this range at the LHC would raise hopes that $W^\pm H^\mp$ production would be observable at the ILC with an integrated luminosity of the order of 1000 events/fb.

As in scan 1 it turns out that the mixing parameters in the third-generation squark sector are important for the understanding of the large cross-section regions. Figure 10a shows that the largest cross-section values lie roughly on two broad stripes with $1 < |\hat{X}_t| < 2.5$ in the $\hat{X}_t$–$\hat{X}_b$ plane leaving the central part of the plane with values below 0.01 fb. We find cross-section values above 0.1 fb only for scenarios that also have a considerable amount of sbottom mixing, typically $\hat{X}_b \lesssim -50$. This can be understood by two observations. Firstly, stop–sbottom threshold enhancement of the cross section needs a low-enough sfermion mass scale or enough mass splitting in the stop or sbottom sector such that $m_{\tilde{t}_1} + m_{\tilde{b}_1}$ can be of the order of $m_{H^\pm}$. Secondly, large values of X_t and X_b entail large values of μ and/or the soft-breaking couplings A_t and A_b, which lead to higher cross-section values.

Motivated by this observations, we study the dimensionless quantity

$$\hat{X}_{tb} := \sqrt{\left(\frac{m_t X_t}{M_{\tilde{f}}^2}\right)^2 + \left(\frac{m_b X_b}{M_{\tilde{f}}^2}\right)^2} \tag{21}$$

as a discriminating variable for our original scan 2. This quantity is just the off-diagonal entries in the stop and sbottom mass matrices, $m_t X_t$ and $m_b X_b$ respectively, added in quadrature and normalised to the common sfermion mass scale $M_{\tilde{f}}$. Figure 10b shows the projection in the $M_{\tilde{f}}$–$\hat{X}_{tb}$ plane. Cross sections above 0.1 fb require $\hat{X}_{tb} \gtrsim 0.8$ and centre roughly around $\hat{X}_{tb} \approx 1$.

For reasons of economy of calculation and interpretation, all our MSSM results were obtained assuming the presence of one common sfermion mass scale $M_{\tilde{f}}$ in the model. Having identified the major enhancement mechanisms of the cross section as threshold effects and large couplings of virtual third-generation squarks, we would like to comment on the more general case of non-uniform sfermion mass-parameter assignments. In our restricted choice of sfermion mass-parameters, given a certain mass scale $M_{\tilde{f}}$, one needs significant amounts of mixing in the stop and sbottom sector in order to fulfill the threshold requirement $m_{\tilde{t}_1} + m_{\tilde{b}_1} \approx m_{H^{\pm}}$ if $M_{\tilde{f}}$ is much larger than $m_{H^{\pm}}/2$. With rising $M_{\tilde{f}}$ this will eventually run into trouble with the parameter restrictions. The amount of squark mixing needed to fulfill the threshold requirement may be relaxed if there is additional mass splitting in the stop and/or bottom sector present through a non-uniform choice of the three third-generation sfermion mass-parameters $M_{\tilde{Q}}$, $M_{\tilde{D}}$, and $M_{\tilde{U}}$.

4 Conclusions

The production of a charged Higgs boson $H^{\pm}$ in association with an electroweak boson $W^{\mp}$ in e^+e^- collisions is a loop-induced process. At the ILC, this process is particularly important for the charged-Higgs-boson detection if pair production is kinematically forbidden. Furthermore, one would gain valuable information about the underlying model by observing this process at the ILC. We calculated the cross section for this process at one-loop order in the framework of the MSSM and THDM and investigated the predictions of both models at an ILC with 500 GeV and 1000 GeV centre-of-mass energy. The MSSM scenarios with large third-generation squark mixing and low sfermion mass scale, for which we showed examples, can give rise to a cross section that differs from a THDM with identical Higgs sector parameters by two orders of magnitude. The dominant enhancement mechanism is threshold effects in stop–sbottom loop graphs if $m_{\tilde{t}_1} + m_{\tilde{b}_1} \approx m_{H^{\pm}}$. Using polarised electron and positron beams can increase the cross section by a factor of 2 to 4 depending on $m_{H^{\pm}}$ and $\tan\beta$. We performed a MSSM parameter scan for regions of large cross section assuming a 1 TeV collider and a charged Higgs boson too heavy to be pair produced at such a machine. We find scenarios with a cross section above 0.1 fb for $m_{H^{\pm}}$ up to about 750 GeV in the whole scanned $\tan\beta$ range $(1 \ldots 50)$. These scenarios require a sfermion mass scale between 200 GeV and 600 GeV and a certain amount of mixing in the stop and sbottom sector. The FORTRAN program 'eeWH' for the calculation of the MSSM and THDM cross sections including the option to perform parameter scans can be obtained from one of the authors[11].

Acknowledgements. We thank Wolfgang Hollik for useful comments. Furthermore, we thank Rachid Benbrik and Sven Heinemeyer for suggesting to improve on the MSSM parameter restrictions we take into account.

References

1. The ATLAS Collaboration, ATLAS Physics Technical Design Report, CERN/LHCC 99-14
2. The CMS Collaboration, CMS Physics Technical Design Report: Vol. II (PTDR2), CERN-LHCC-2006-021
3. The ATLAS and CMS Collaborations, J.G. Branson, D. Denegri, I. Hinchliffe, F. Gianotti, F.E. Paige, P. Sphicas (Eds.), hep-ph/0110021
4. V. Büscher, K. Jakobs, Int. J. Mod. Phys. A **20**, 2523 (2005) [hep-ph/0504099]
5. ECFA/DESY LC Physics Working Group Collaboration, J.A. Aguilar-Saavedra et al., hep-ph/0106315
6. ACFA Linear Collider Working Group, K. Abe et al., hep-ph/0109166
7. American Linear Collider Working Group, T. Abe et al., hep-ex/0106056
8. D. Denegri et al., hep-ph/0112045
9. K.A. Assamagan, Y. Coadou, A. Deandrea, Eur. Phys. J. direct C **4**, 9 (2002) [hep-ph/0203121]
10. J. Kalinowski, S. Pokorski, Phys. Lett. B **219**, 116 (1989)
11. A. Gutierrez-Rodriguez, O.A. Sampayo, Phys. Rev. D **62**, 055 004 (2000)
12. A. Gutierrez-Rodriguez, M.A. Hernandez-Ruiz, O.A. Sampayo, Rev. Mex. Fis. **48**, 413 (2002) [hep-ph/0110289]
13. S. Kanemura, S. Moretti, K. Odagiri, JHEP **0102**, 011 (2001) [hep-ph/0012030]
14. A. Djouadi, J. Kalinowski, P.M. Zerwas, Z. Phys. C **54**, 255 (1992)
15. B.A. Kniehl, F. Madricardo, M. Steinhauser, Phys. Rev. D **66**, 054 016 (2002) [hep-ph/0205312]
16. S. Moretti, Eur. Phys. J. C **34**, 157 (2004) [hep-ph/0306297]
17. T. Farris, H.E. Logan, S. Su, Phys. Rev. D **69**, 035 005 (2004) [hep-ph/0308124]
18. O. Brein, T. Hahn, S. Heinemeyer, G. Weiglein, in: Proc. of the 10th International Conference On Supersymmetry And Unification Of Fundamental Interactions (SUSY02) (DESY, Hamburg, 2002) hep-ph/0402053
19. H.E. Logan, S. Su, Phys. Rev. D **66**, 035 001 (2002) [hep-ph/0203270]
20. H.E. Logan, S. Su, Phys. Rev. D **67**, 017 703 (2003) [hep-ph/0206135]
21. S.H. Zhu, hep-ph/9901221
22. S. Kanemura, Eur. Phys. J. C **17**, 473 (2000) [hep-ph/9911541]
23. A. Arhrib, M. Capdequi Peyranere, W. Hollik, G. Moultaka, Nucl. Phys. B **581**, 34 (2000) [hep-ph/9912527]
24. O. Brein, in: Proc. of the 10th International Conference On Supersymmetry And Unification Of Fundamental Interactions (SUSY02) (DESY, Hamburg, 2002), hep-ph/0209124
25. S. Su, private communication, 2002
26. J.A. Grifols, A. Mendez, Phys. Rev. D **22**, 1725 (1980)
27. M. Böhm, W. Hollik, H. Spiesberger, Fortschr. Phys. **34**, 687 (1986)
28. P.H. Chankowski, S. Pokorski, J. Rosiek, Nucl. Phys. B **423**, 437 (1994) [hep-ph/9303309]
29. A. Dabelstein, Z. Phys. C **67**, 495 (1995) [hep-ph/9409375]
30. J.A. Coarasa, D. Garcia, J. Guasch, R.A. Jimenez, J. Sola, Eur. Phys. J. C **2**, 373 (1998) [hep-ph/9607485]
31. F. del Aguila, A. Culatti, R. Munoz-Tapia, M. Perez-Victoria, Phys. Lett. B **419**, 263 (1998) [hep-th/9709067]
32. F. del Aguila, M. Perez-Victoria, Acta Phys. Pol. B **28**, 2279 (1997) [hep-ph/9710442]
33. J. Küblbeck, M. Böhm, A. Denner, Comput. Phys. Commun. **60**, 165 (1990)
34. H. Eck, Ph.D. thesis, University of Würzburg (1995)
35. T. Hahn, M. Perez-Victoria, Comput. Phys. Commun. **118**, 153 (1999) [hep-ph/9807565]

---

[11] Please use the e-mail address oliver.brein@durham.ac.uk.

36. T. Hahn, Comput. Phys. Commun. **140**, 418 (2001) [hep-ph/0012260]
37. T. Hahn, C. Schappacher, Comput. Phys. Commun. **143**, 54 (2002) [hep-ph/0105349]
38. ALEPH Collaboration, S. Schael et al., Eur. Phys. J. C **47**, 547 (2006)
39. S. Heinemeyer, W. Hollik, G. Weiglein, Eur. Phys. J. C **9**, 343 (1999)
40. S. Heinemeyer, Comput. Phys. Commun. **124**, 76 (2000)
41. G. Degrassi, S. Heinemeyer, W. Hollik, P. Slavich, G. Weiglein, Eur. Phys. J. C **28**, 133 (2003)
42. M. Frank, T. Hahn, S. Heinemeyer, W. Hollik, H. Rzehak, G. Weiglein, hep-ph/0611326
43. A.L. Kagan, M. Neubert, Phys. Rev. D **58**, 094 012 (1998)
44. A.L. Kagan, Eur. Phys. J. C **7**, 5 (1999)
45. T. Hahn, W. Hollik, J.I. Illana, S. Peñaranda, hep-ph/0512315
46. CLEO Collaboration, S. Chen et al., Phys. Rev. Lett. **87**, 251807 (2001)
47. BABAR Collaboration, B. Aubert et al., hep-ex/0207074
48. Heavy Flavor Averaging Group (HFAG), E. Barberio et al., hep-ex/0603003
49. S. Heinemeyer, W. Hollik, G. Weiglein, Phys. Rep. **425**, 265 (2006)
50. M. Misiak et al., Phys. Rev. Lett. **98**, 022 002 (2007)
51. Particle Data Group Collaboration, S. Eidelman et al., Phys. Lett. B **592**, 1 (2004)
52. Muon g-2 Collaboration, G.W. Bennett et al., Phys. Rev. Lett. **89**, 101 804 (2002)
53. Muon g-2 Collaboration, G.W. Bennett et al., Phys. Rev. Lett. **89**, 129 903 (2002)
54. Muon g-2 Collaboration, G.W. Bennett et al., Phys. Rev. Lett. **92**, 161 802 (2004)
55. S. Heinemeyer, D. Stöckinger, G. Weiglein, Nucl. Phys. B **690**, 62 (2004)
56. S. Heinemeyer, Nucl. Phys. B **699**, 103 (2004)
57. T. Moroi, Phys. Rev. D **53**, 6565 (1996)
58. T. Moroi, Phys. Rev. D **56**, 4424 (1997)
59. M. Carena, S. Heinemeyer, C.E.M. Wagner, G. Weiglein, Eur. Phys. J. C **26**, 601 (2003)
60. O. Brein, W. Hollik, Eur. Phys. J. C **13**, 175 (2000)
61. O. Brein, W. Hollik, S. Kanemura, Phys. Rev. D **63**, 095 001 (2001) [hep-ph/0008308]
62. O. Brein, Comput. Phys. Commun. **170**, 42 (2005) [hep-ph/0407340]
63. G.P. Lepage, J. Comput. Phys. **27**, 192 (1978)
64. G.P. Lepage, Report CLNS-80/447 (Cornell University, LNS)
65. http://www.ippp.dur.ac.uk/∼obr/eeWH-scan/
66. LEP Working Group for Higgs boson searches, R. Barate et al., Phys. Lett. B **565**, 61 (2003)